International Journal of Fatigue 116 (2018) 106–117

Contents lists available at ScienceDirect

International Journal of Fatigue

journal homepage: www.elsevier.com/locate/ijfatigue

Effect of stress state and simultaneous hot corrosion on the crack propagation and fatigue life of single crystal superalloy CMSX-4

L. Brooking[a,*], S. Gray[a], J. Sumner[a], J.R. Nicholls[a], G. Marchant[b], N.J. Simms[a]

[a] Cranfield University, College Rd, Cranfield MK43 OAL, United Kingdom
[b] Siemens Industrial Turbomachinery, 1 Waterside S, Lincoln LN5 7FD, United Kingdom

ARTICLE INFO

Keywords:
Hot corrosion
Fracture mechanics
FEA
Single crystal superalloys

ABSTRACT

Operating conditions within industrial gas turbines are changing in response to pressures to reduce environmental impact and enable use of renewable sources. This is driving an increase in the operational temperatures and pressures of combustion in turbine systems. Additionally, diverse operating environments can result in higher sulphur and trace metal contaminant levels, exacerbating hot corrosion in GT systems. Low cycle fatigue (LCF) cycling can also be intensified as a result of increased start/stop shutdowns. The combined effects of hot corrosion and stress are experimentally studied on CMSX-4 single crystal (SC) γ/γ' system under both fatigue and static stress conditions, with either a multi-axial bending or uniaxial stress state. The associated stress intensity thresholds (K_{TH}) under the various stress conditions were evaluated using finite element analysis (FEA). Cracking was observed both under static and fatigue stress conditions in a hot corrosion environment. Crack morphologies were analysed using SEM techniques. Bending stresses and fatigue cycles demonstrated increased crack propagation in the presence of hot corrosion with static uniaxial stresses showing the longest nucleation times and lowest propagation rates.

1. Introduction

Developments to improve the operational efficiencies of gas turbines (GT) in recent times have led to increases in the operational temperatures of turbine blade components. Type II hot corrosion is caused by the formation of an $Na_2SO_4/CoSO_4$ eutectic on the surface, resulting in pitting type attack [1]. Whilst turbines are designed to operate outside of the corrosion temperature ranges, it is thought that type II hot corrosion can be assisted by local stress and strain. As such, cracking and degradation mechanisms not accounted for by current design life models [2,3] have been observed in regions such as the under-platform area. It is proposed that this is due to such locations being subject to simultaneous high stresses and corrosive conditions, resulting in a hot corrosion assisted fracture and/or fatigue mechanism.

The superalloy CMSX-4 is an example of a 1st stage turbine blade alloy with a single crystal γ/γ' system. CMSX-4 has favourable high temperature creep and rupture properties combined with good production affordability when compared with other single crystal (SC) superalloys [4]. However its lower Cr content compromises its corrosion resistance. As such CMSX-4 is susceptible to hot corrosion at temperatures below type II reported at 680–800 °C [5,6]. It has been reported that type II hot corrosion can occur at temperatures as low as 575 °C [7]. The impact of static stress assisted hot corrosion on CMSX-4 was studied in previous work and was found to occur at a temperature of 550 °C [8], also supported by [2]. It was demonstrated in this work [8], that a type II mechanism can occur at these lower temperatures when assisted by stress. Additionally a switch in the corrosion mechanism from attack of the γ at locations towards the specimen surface to attack of the γ' at the stress assisted crack tip was observed.

It was further observed that cracks appear to then subsequently interact with and split γ' precipitates. Resulting in propagation along {1 0 0} planes perpendicular to the specimen surface. Without the presence of hot corrosion, cracks in a uniaxial stress state propagate and fracture along slip bands of the {1 1 1} family [9–11] in SC superalloys such as CMSX-4 at temperatures up to 850 °C. In complex multi axial stress states for low ΔK levels cracks propagate along macroscopic {1 0 0} or {1 1 0} planes due to opposing slip contributions from the {1 1 1} slip systems, at higher ΔK levels they propagate along {1 1 1} systems [12].

A detrimental effect of hot corrosion on the fatigue life of superalloys has been observed in previous research [2,13–16]. It can also be concluded from these works that the longer the duration of the fatigue testing, the greater the relative effect of hot corrosion on reducing fatigue life. However the effects of multi-axial stress states and static stress gradients

* Corresponding author.
E-mail address: l.b.brooking@cranfield.ac.uk (L. Brooking).

https://doi.org/10.1016/j.ijfatigue.2018.05.002
Received 27 March 2018; Received in revised form 1 May 2018; Accepted 2 May 2018
Available online 03 May 2018

Nomenclature and units

K	stress intensity ($Pa{\cdot}m^{1/2}$)
K_{TH}	fatigue stress intensity threshold
K_{cr}	critical stress intensity threshold
K_I	mode I stress intensity
σ	stress (Pa)
Y	linear elastic fracture mechanics geometry factor
C	Paris law constant
n	Paris law exponent
J	J-integral (J/m^2)
x, y, z	Cartesian coordinates
ν	Poisson's ratio
E	Young's modulus (Pa)
σ_G	stress gradient parameter (Pa/m)
σ_A	specimen surface stress at location A (Pa)
σ_B	specimen surface stress at location B directly opposite A (Pa)
t_{AB}	specimen thickness from A-B (m)

on crack propagation in superalloys, combined with hot corrosion fatigue, is not well studied. A study into the effects of stress state on the fatigue crack growth in polycrystalline Inconel 718 exposed to an oxidising environment, found that with increased oxidation cracks became less influenced by stress intensity (ΔK) and more by stress state [17]. With many superalloys such as CMSX-4 demonstrating anisotropic behaviour [11,9], and the under-platform region of GT blades being under a multiaxial bending stress [18], it is important to develop an understanding of the materials behaviour under these combined conditions.

Finite element analysis (FEA) uses computational solvers to solve a chain of simultaneous equations in order to calculate the local stresses within a defined geometry mesh subjected to boundary conditions. FEA combined with linear elastic fracture mechanics (LEFM) provides a capable tool to assess crack stability and propagation for fatigue that follows Paris' law behaviour [19].

This paper proposes a combined mechanism for fracture under type II hot corrosion conditions, the mechanism is based upon the following fracture principles. Firstly under static load conditions the local stress intensity (K_I) has to overcome the critical stress threshold of the material (K_{cr}), resulting in the complete fracture of a brittle body or a body under plane strain conditions. Secondly Paris-law fatigue propagation occurs as a result of the change in stress intensity (ΔK) which exceeds the fatigue threshold (K_{TH}). The proposed mechanism works on the observation that hot corrosion had the impact of locally lowering both the K_{cr} critical fracture threshold and the fatigue threshold K_{th} at the crack tip. Therefore blades subject to hot corrosion conditions in highly stressed regions can undergo localised fracture due to a combination of static stress-hot corrosion cracking and accelerated Paris fatigue cracking, resulting in accelerated combined crack propagation similar to the SCC mechanism proposed by [20]. Additionally stop start type environmental fatigue models have been proposed, these mechanisms are based on the time dependant nature of species diffusing ahead of the crack tip causing embrittlement [21].

2. Experimental

2.1. Material

The single crystal superalloy CMSX-4 (Table 1) was used to produce all the samples for this paper. The samples were machined from directionally solidified bars such that the orientations given in Fig. 1 were controlled for specific specimen geometries. Literature suggests that the fatigue stress intensity threshold for CMSX-4 in air is around 15 $MPa{\cdot}m^{1/2}$ [12]. The critical stress intensity threshold is given in air at 650 °C as 60 $MPa{\cdot}m^{1/2}$ [22].

2.2. Experimental methodologies

The corrosive deposit flux used for experimental testing was maintained through a deposit recoat methodology, where recoats were applied every 100 h. The salt used was an 80/20 mol% mix of Na_2SO_4 - K_2SO_4 and all tests were conducted at 550 °C with a test gas of 300 ppm SO_2 and air. The sulphate salt deposit and test gas was used in order to simulate sulphidation or low temperature hot corrosion as seen in a GTs. Testing systematically varied the stress state and deposit flux. A balance accurate to 0.01 mg was used to measure the salt quantities deposited.

Table 1
Composition of CMSX-4 (wt%).

Alloy	Cr	W	Co	Mo	Al	Ti	Ta	Re	Hf	Ni
CMSX-4	6.5	6.0	9.6	0.6	5.6	1.0	6.5	3.0	0.1	Bal.

Three geometries were used for static testing: C-rings, 3-point bend specimens and plain geometry fatigue specimens (Fig. 2). This was in order to achieve three different stress states: multi-axial high stress gradient, multi-axial high von Mises and uniaxial uniform tensile stress state.

Target stresses for C-rings and three point bend specimens were achieved by tensioning to calculated displacements using equations from standards [23,24] respectively. Statically loaded specimens were checked for cracking using an optical microscope every 100 h. If no cracking was detected using an optical microscope then specimens were re-salted checked for relaxation and further exposed in 100 h intervals.

Additional statically stressed C-ring tests were run, where tests were systematically terminated at 100,300 and 500 h in order to assess crack damage and propagation as a function of time and stress. This was achieved through measuring the {1 0 0} corrosion driven crack planes and crack initiation points.

Fatigue specimens were tested until failure, testing was conducted using a load-controlled fatigue rig equipped with induction heating. The induction system heated a sheath around the fatigue specimens in order to maintain a more consistent temperature across the specimen. Cycles to failure (S-N) graphs were produced for a range of tensile stresses where R = 0 using a trapezoidal wave form. Samples were exposed for 500 h of pre-corrosion prior to fatigue testing, this was done with one of two set pre corrosion fluxes of 1.25 $\mu g/cm^2/h$ or 5 $\mu g/cm^2/h$ representative of a lower and higher under platform deposit flux.

2.3. Analytical methodologies

Optical microscopy and field electron gun (FEG) SEM imaging techniques were used to study and characterise samples post exposure. Image-J [25] image processing software was used to take measurements from images, such as crack size and depth, and AZtec [26] was used to process EDX data.

FEG SEM microscopy was conducted on both Phillips FEI XL-30 and JEOL 7800F systems. Specimen surfaces, and fracture surfaces were

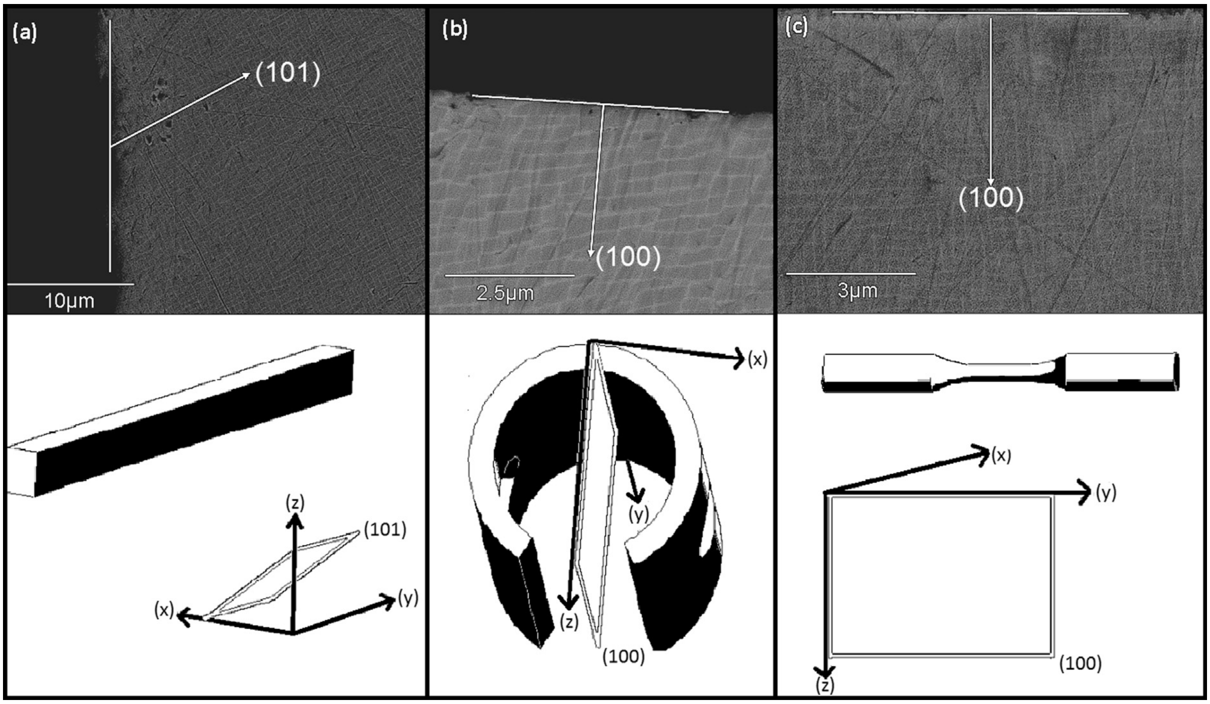

Fig. 1. Microstructure orientation determined from backscatter SEM images showing γ/γ' orientation in relation to specimen surface. The crystallographic orientation is illustrated/defined within the geometry axis below the relevant SEM image, (a) three point bend 30°–45° (2 0 1)-(1 0 1), (b) C-ring 90° (1 0 0), (c) plain specimen 90° (1 0 0).

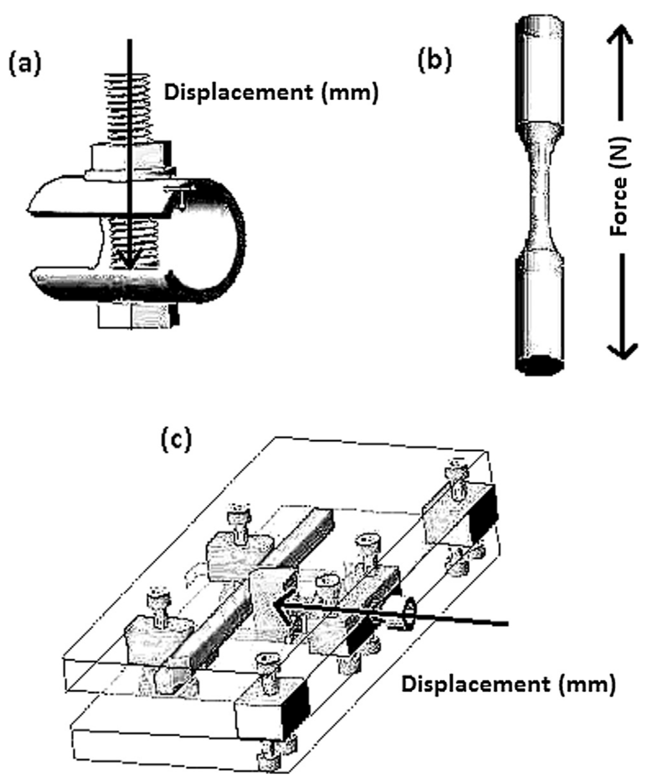

Fig. 2. Specimen geometry loadings shown through illustration, (a) C-ring strain control, (b) plain specimen load control, (c) 3-point bend strain control.

analysed before being prepared by mounting in a 50:50 mixture of epoxy resin and ballotoni (40–70 μm diameter glass beads). They were then cross sectioned, ground and polished in oil to preserve corrosion products, enabling crack tip and microstructure analysis.

Crack size measurements were spilt into three parameters, crack depth was defined as the [1 0 0] propagation depth into the specimen. Crack width was measured as the total width of all joined thumbnail cracks on the {1 0 0} plane if multiple initiations were visible on the fracture face. The crack rate of initiation and propagation for static stress conditions was calculated as the average [1 0 0] crack depth over the total test duration. The {1 0 0} area was calculated as half of an ellipse making an individual thumbnail fracture, these were added where multiple {1 0 0} fractures were visible.

FEA was conducted using ANSYS R15 [27] and ABAQUS [28]. An idealised isotropic material model was used for the ⟨0 0 1⟩ direction, this was derived from published data [9]. 3D models were used to assess the axial directions and magnitudes of the stresses within the three geometries. Additionally the J-integral energies were calculated for cracks propagating in the [1 0 0] crystallographic direction using 2D models. Boundary conditions for FEA modelling were set up to represent the experimental parameters where strain control was represented by a displacement boundary condition and load control by a load boundary condition. In order to quantify the stress gradient present in the geometries, a macro stress gradient parameter is proposed (Eq. (1)).

Stress gradient parameter:

$$\sigma_G = (\sigma_A - \sigma_B)/t_{AB} \tag{1}$$

Table 2
Stress states present in the three specimen geometries.

Geometry	Target stress (MPa)	Principal (mode 1) tension (MPa)	Principal (mode 1) compression (MPa)	Principal stress gradient parameter (σ_G) (MPa/mm)	von Mises tension (MPa)
Plain specimen	800	800	0	0	800
C-ring	800	935	−1100	127.19	820
Three point bend	800	880	−980	31	849

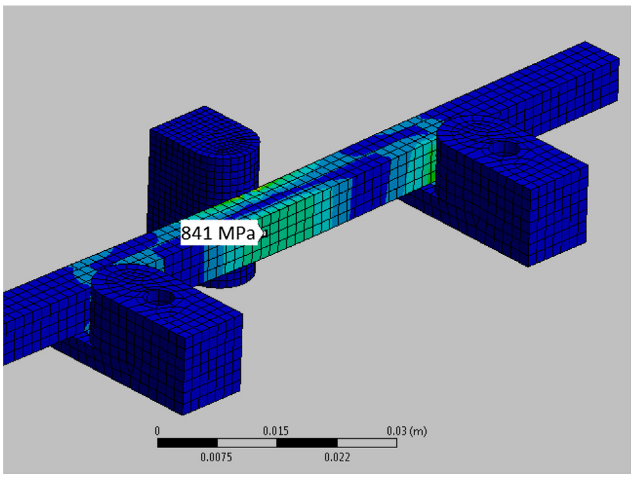

Fig. 3. FE model of von-Mises stress distribution in three point bend geometry, showing elevated compressive stresses at contact point with roller.

3. Theory/calculation

The general LEFM (Eq. (2)) was used as a model to assess crack stability and growth and determine threshold crack lengths. LEFM assess crack stability as a function of the macroscopic elastic stress field (σ) crack length (a) and geometry factor (Y).

Linear elastic fracture mechanics equation [29]:

$$K = \sigma Y\sqrt{a\pi} \tag{2}$$

The Paris law (Eq. (3)) is then commonly used to model crack propagation da/dN as a function of the change in stress intensity (ΔK), constant (C) and an exponent (n).

Paris law crack growth equation [29]:

$$\frac{\partial a}{\partial N} = C(\Delta K)^n \tag{3}$$

4. Results and discussion

4.1. Static stress results and discussion

In the C-ring geometry modelling predicted that the principal compressive stresses are relatively higher than the tensile equivalents. This can be explained by the smaller inner circumference producing a larger compressive strain and resultant stress than the relatively larger outer circumference in tension. Similarly modelling predicted higher compressive stresses in the three point bend specimen relative to the tensile equivalents. However these results are associated to the additional contact force of the three point bend roller at the point of maximum compressive deflection.

Table 3
Static stress, exposure for visible cracking.

Geometry	Deposition flux (µg/cm^2/h)	Stress (MPa)	Time to crack 100 h intervals (hours)
C-ring	5	800	100
C-ring	5	700	100
C-ring	5	500	200
C-ring	1.25	800	100
C-ring	1.25	700	200
C-ring	1.25	500	300
Plain specimen	5	800	300
Plain specimen	1.25	800	No cracking after 200
Plain specimen	5	900	200
Three point bend	5	800	200

Table 2 Presents a summary of the predicted maximum principal stress, the stress gradient parameter and von Mises surface stresses present in the three geometries. This is given as a function of the target stress which was the stress used to calculate the displacement required from the relevant standard. These stress components were calculated using FEA, the specimen loading is defined in Fig. 2 and an example FE model is presented in Fig. 3. Comparing the stress conditions of the three geometries presented in Table 2, shows that C-rings provide both the highest stress gradient and the highest (mode I) principal crack opening stress, the three point bend geometry however produces the highest localised von Mises stress. In the C-ring geometry modelling predicted that the principal compressive stresses are relatively higher than the tensile equivalents. This can be explained by the smaller inner circumference producing a larger compressive strain and resultant stress than the relatively larger outer circumference in tension. Similarly modelling predicted higher compressive stresses in the three point bend specimen relative to the tensile equivalents. However these results are associated to the additional contact force of the three point bend roller at the point of maximum compressive deflection.

The static stress hot corrosion results presented in Table 3 suggest a time dependant cracking mechanism. Stress induced hot corrosion cracks generated in these static stress environments all followed an orthogonal microstructure plane as shown in Fig. 4. It is hypothesised that this occurs as a result of a localised reduction in K_{cr} (embrittlement) of the γ' at or ahead of the crack tip, with the next closest γ' to be embrittled being orthogonal to the crack tip, as illustrated in Fig. 5.

The results demonstrate that C-rings induce the most aggressive stress state for static stress-hot corrosion as they produced optically visible cracking after the shortest exposure times. The second most aggressive stress state tested was the three point bend specimen with this specimen showing cracking 100 h after the comparable C-ring specimen. Plain specimens required longer exposure times in order to crack still, cracking a further 100 h after the comparable three point bend specimen. These results suggest a trend that the static stress hot corrosion cracking mechanism was exacerbated by the magnitude of

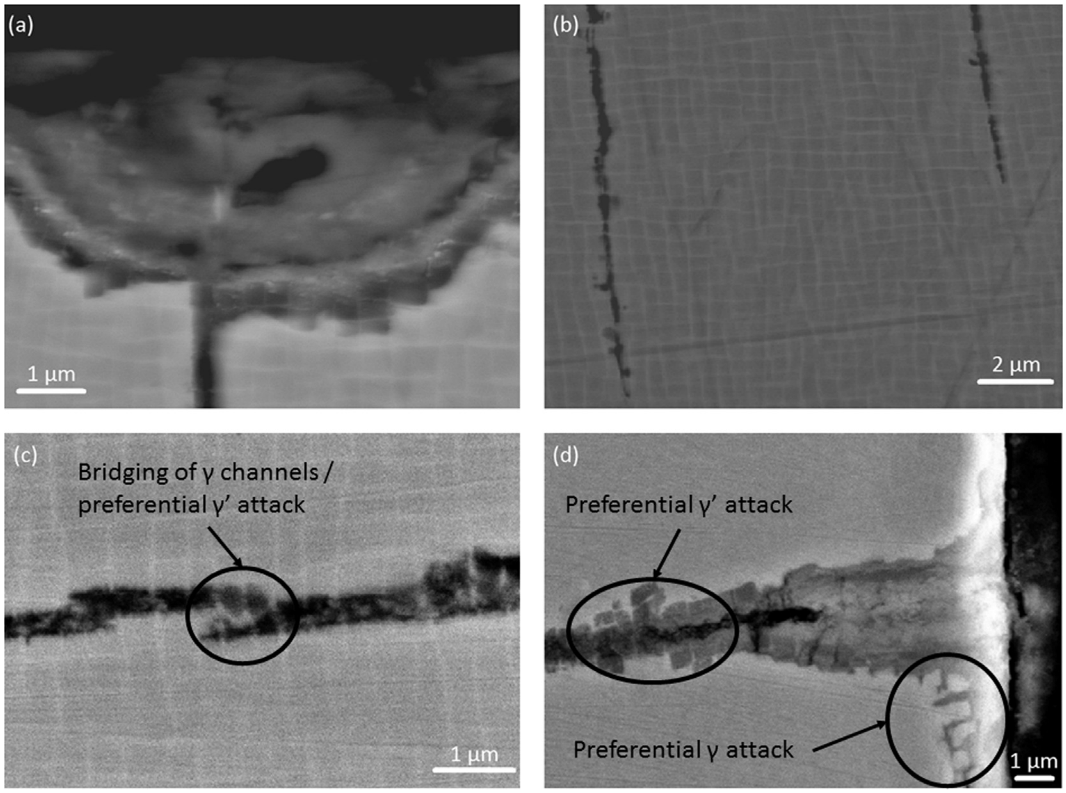

Fig. 4. SEM micro section images of statically loaded specimens, (a) & (b) back scattered SEM images of a three point bend specimen, 800 MPa statically loaded, 200 h, 5 µg/cm^2/h flux, 550 °C, showing a crack initiating from an apparent corrosion pit corroding and propagating through γ' precipitates, (c) secondary SEM images of a C-ring, 800 MPa statically loaded, 100 h, 5 µg/cm^2/h flux, 550 °C, showing preferential γ' attack down the crack with cracks, with cracks propagating through γ' leaving γ channel bridging, (d) back scattered SEM image showing preferential γ attack towards the stress relaxed surface and preferential γ' attack further down the crack.

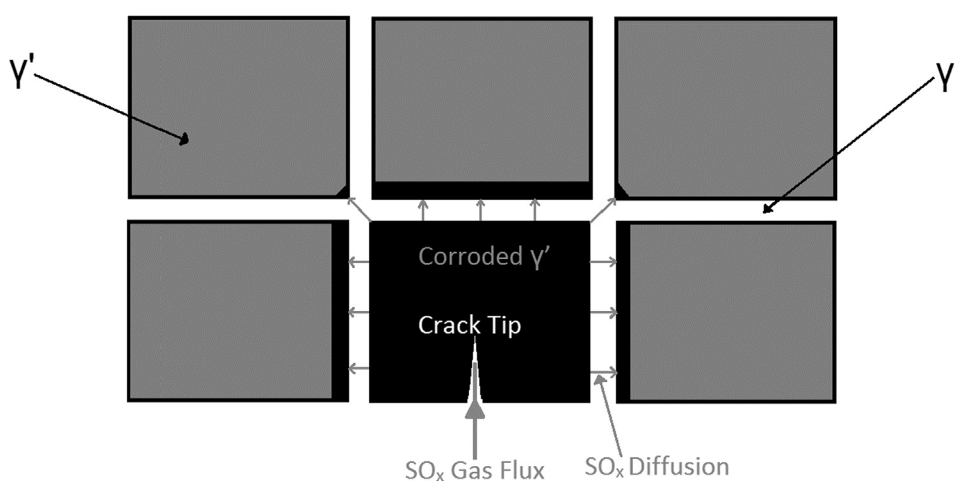

Fig. 5. Proposed mechanism for gas induced fluxing at the crack tip, showing stress assisted corrosive species diffusion into the γ' and resulting in orthogonal embrittlement and thus crack propagation.

the stress gradient induced through bending. The plain specimen tested for 200 h at 800 MPa and a 1.25 µg/cm^2/h flux was further cross sectioned and examined under an SEM to look for microscopic crack initiations, however no initiations or cracks could be found on this specimen, implying stress and flux are crucial in order for this mechanism to occur.

Optical image analysis of the (1 0 0) thumb nail fracture surfaces on C-rings after set exposures allowed for the calculation of the average static stress crack initiation and propagation rates over the exposure duration, these are presented in Table 4.

For C-rings crack propagation rates decrease as cracks propagate through the C-ring section. This is likely due to a couple of reasons:

Table 4
Static stress crack propagation rates of C-rings and plain specimens subject to specific exposure intervals.

Geometry	Target stress (MPa)	Exposure time (h)	Flux (μg/cm^2/h)	[1 0 0] Crack depth (mm)	AVE da/dt (μm/h)
C-ring	800	100	5	0.46	4.6
C-ring	800	500	5	1.45	2.9
C-ring	700	300	5	0.97	3.2
C-ring	700	500	5	1.35	2.7
Plain specimen	900	200	5	0.398	1.9
Plain specimen	800	300	5	0.519	1.73

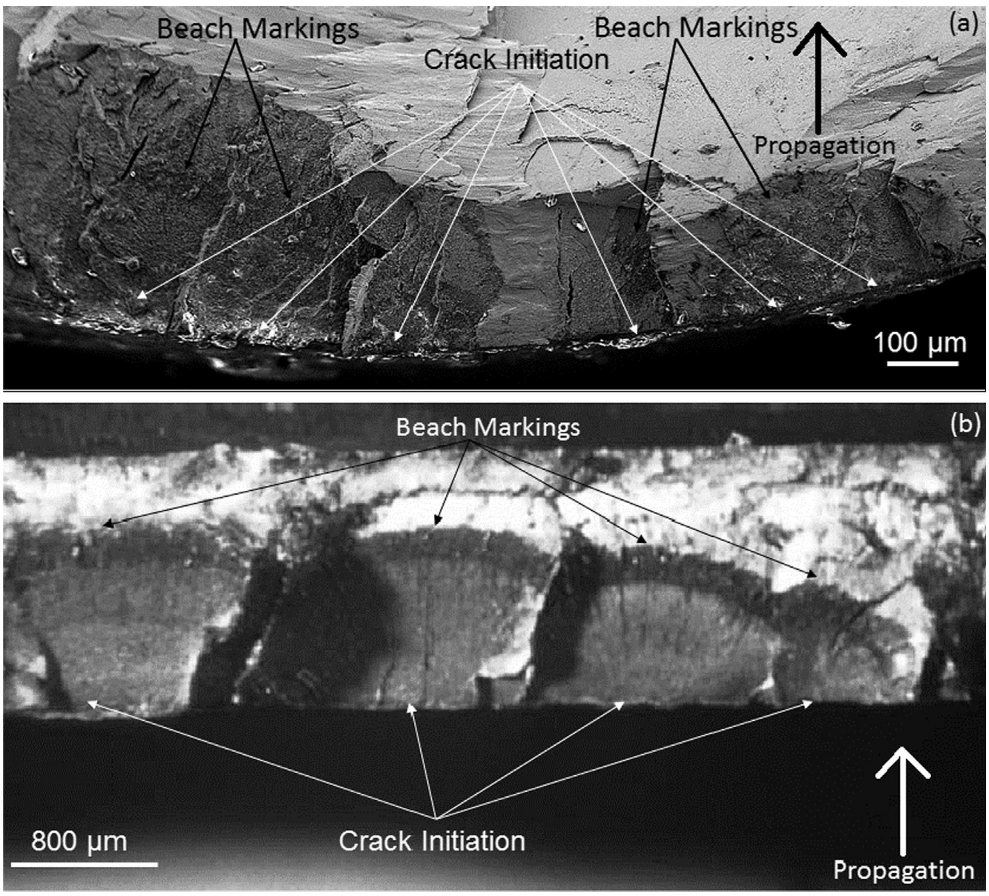

Fig. 6. Microscope images of statically loaded specimen fracture faces, (a) secondary electron SEM image of a 900 MPa, 5 μg/cm^2/h flux, 550 °C, 200 h, statically loaded plain specimen [0 0 1] propagation (b) optical image of a 500 MPa, 5 μg/cm^2/h flux, 550 °C, 100 h, statically loaded C-ring specimen [0 0 1] propagation markings.

firstly because as the crack propagates the stress gradient at the crack tip reduces; and secondly because of stress relaxation due to the presence of the crack.

In C-rings, static stress cracks form a broad fronted propagation generated from multiple initiations, which results in conjoined thumbnail cracks right across the specimen width. Whereas in statically loaded plain specimens cracks form a similar morphology but propagate and initiate at a slower rate (Fig. 6). Both optical and SEM analysis of the fracture surfaces of statically loaded specimens show beach type markings on the fracture faces. These are associated to the "stop-start" time dependant nature of hot corrosion stress cracking, however the exact mechanism needs further study to fully explain the changes in growth rate.

Under static conditions a conventional form of type II hot corrosion occurred on the specimen surface forming a Co/Ni rich outer oxide scale. In addition an inner Al/Cr rich mixture of oxides and the salts K_2SO_4 and Na_2SO_4 formed. Whilst the temperature of 550 °C is considered too low to form the eutectic mixtures required for type II hot corrosion, in a stress assisted system the corrosion mechanism appears to be consistent with type II (Fig. 7). At the crack tip however, the corrosion mechanism seems to switch and interact with the γ' precipitates. It is hypothesised that this could be due to a change in the fluxing mechanism. As the sulphate salt species are not mobile enough to travel down the crack, it is proposed that the fluxing mechanism at the crack tip occurs through the stress assisted diffusion of SO_x and potentially other corrosive species into the γ' precipitates.

4.2. Fatigue results and discussion

Two experimental S-N curves are presented in Fig. 8 for a 1.25 and a 5 μg/cm^2/h deposition flux for CMSX-4 pre corroded for 500 h at 550 °C. The tabulated experimental results are given in (Table 5). Both deposition fluxes fail in fewer cycles than the predicted baseline fatigue data in air.

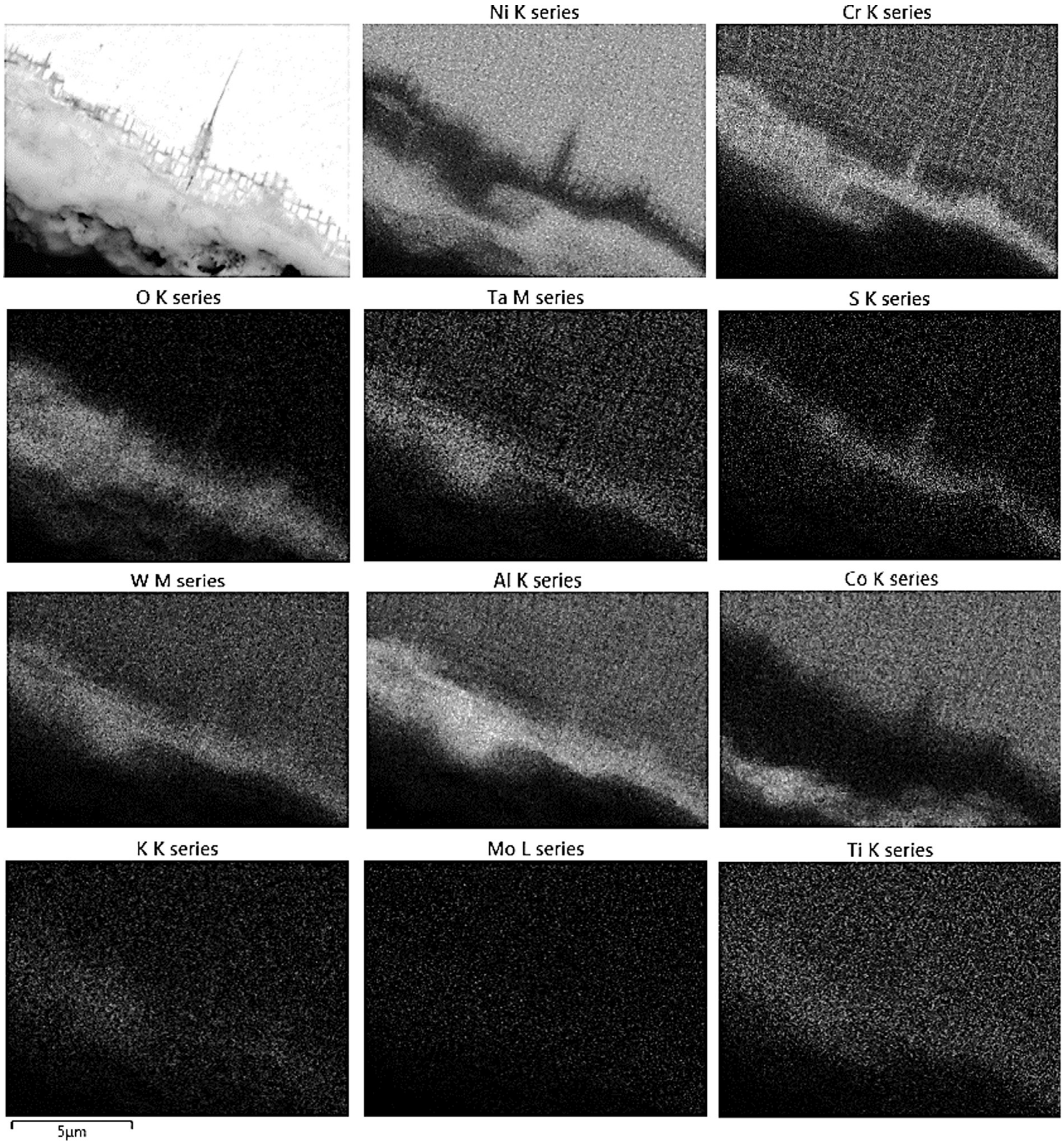

Fig. 7. C-ring exposed for 300 h at 800 MPa, and 5 μg/cm^2/h, shows segregation of elements within the corrosion products forming an outer oxide scale of Ni/Co and an inner Cr/Al rich layer with a sulphur rich band reacting with the substrate. Also visible is some elemental segregation in the γ/γ' microstructure showing the γ being rich in Cr and the γ' in Al.

Optical examination of the fracture faces reveal that the 1.25 μg/cm^2/h flux fractured predominately along a conventional (1 1 1) slip plane, whereas 5 μg/cm^2/h flux specimens have a thumb nail feature that failed along the corrosion driven (1 0 0) crack plane. Further adding in a 60 s dwell period with a 1-60-1-1 (s) trapezoidal wave form generates multiple crack initiation points comparable to static stress fracture faces (Fig. 9). These multiple cracks are also visible when viewing the specimen from the side (Fig. 10). The observation of these additional cracks suggests that short cracks are initiating and growing in dwell periods due to a hot corrosion cracking mechanism.

The accelerated failure of fatigue specimens exposed to the lower flux of 1.25 μg/cm^2/h but not exhibiting (1 0 0) fracture features, could be attributed to stress concentration due to pitting from type II corrosion generated during pre-corrosion. It is additionally possible that a reduced K_{TH} is induced at the crack tip but that the fracture is still dominated by (1 1 1) slip planes, however this short crack growth behaviour requires further investigation.

Examining the corrosion fatigue fracture faces under SEM revealed that darkened beach mark type features were visible (Fig. 11), mapping of these markings demonstrates that they are associated with oxygen-rich bands (Fig. 12). These features appear to be too infrequent and have too large a spacing to be associated solely with fatigue "striation"

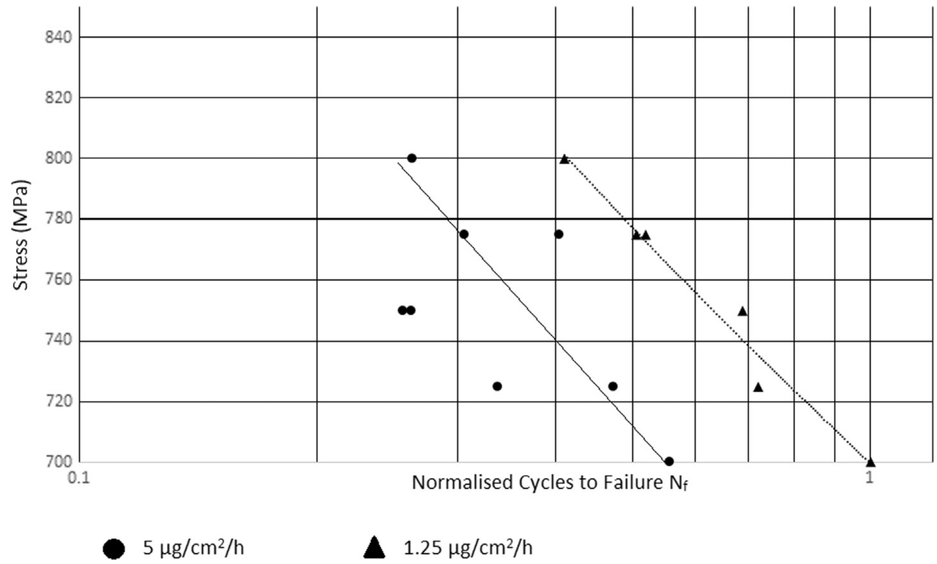

Fig. 8. 1-1-1-1 (s) S-N curves for CMSX-4 with 500 h of 1.25 or 5 μg/cm^2/h pre corrosion flux at 550 °C. This shows a reduction in fatigue life correlating to the salt deposition rate.

Table 5
Trapezoidal wave form fatigue results with 500 h pre corrosion cycles to failure.

R = 0 Stress (MPa)	500 h Pre corrosion (μg/cm^2/h)	[1 0 0] Length (mm)	(1 0 0) Area estimate mm^2	Wave form (s)	Normalised cycles to failure N_f	(1 0 0) Visible crack initiations on fracture face
700	5	1.344	4.10	1-1-1-1	0.557	1
725	5	0.6	0.80	1-1-1-1	0.473	1
725	5	1.23	3.54	1-1-1-1	0.338	1
750	5	0.303	0.35	1-1-1-1	0.256	1
750	5	1.221	2.95	1-1-1-1	0.262	1
775	5	1.538	4.68	1-1-1-1	0.307	1
775	5	0	0	1-1-1-1	0.404	0
800	5	0.711	0.80	1-1-1-1	0.263	1
800	5	0.751	2.74	1-60-1-1	0.0597	9
700	1.25	0	0	1-1-1-1	1.001	0
725	1.25	0	0	1-1-1-1	0.722	0
750	1.25	0	0	1-1-1-1	0.689	0
775	1.25	0	0	1-1-1-1	0.505	0
775	1.25	0	0	1-1-1-1	0.52	0
800	1.25	0	0	1-1-1-1	0.411	0

markings, and are therefore most likely associated with corrosion dwell steps similar to those seen in static stress cracking.

The increased deposition flux rate of 5 μg/cm^2/h exhibited a reduced fatigue life when compared with 1.25 μg/cm^2/h. This reduction in fatigue life was as high as 45% at lower stresses where corrosion had more time to interact with the alloy.

The corrosion mechanisms for fatigue specimens resembled those observed in static stress conditions (Fig. 13). It is similarly hypothesised that the [1 0 0] orthogonal crack growth is driven by gas induced corrosion interacting initially with orthogonal γ' precipitates (Fig. 5). However this is more prevalent at shorter crack lengths or a lower crack tip ΔK, as a higher ΔK exceeding the K_{TH} of the material fail on the conventional [1 1 1] fracture facets causing ridges or rooftops.

4.3. Fracture analysis

The stress intensities for 50 and 10 μm cracks are presented in Table 6 for the three geometries along with the geometry factors. These parameters where calculated from J-integral energies using integrated FE code [28]. For comparison the crack lengths required to exceed the published K_{TH} of 15 MPa·m$^{1/2}$ are also presented.

Review of the fracture mechanics analysis shows that the most aggressive geometry are the C-rings, followed by the plain specimen and lastly the three point bend. The three point bend specimen is likely less aggressive than the plain specimen due to relaxation over the specimen span as a crack initiates and propagates modelling conducted on increasing crack lengths supports this. Conversely the constant uniform stress present in the plain specimen leads to a more conventional increase in stress intensity at the crack tip as a crack propagates.

Comparing the fracture analysis with static stress experimental shows that cracks propagate well below the published K_{cr} of 60 MPa·m$^{1/2}$. Suggesting that localised hot corrosion attack allows the crack to propagate with a static tensile stress present.

Additionally relating the fracture analysis to fatigue testing results demonstrates that fatigue cracks can propagate below the published K_{TH} of 15 MPa·m$^{1/2}$. Suggesting that localised hot corrosion additional has the net effect of reducing the fatigue threshold.

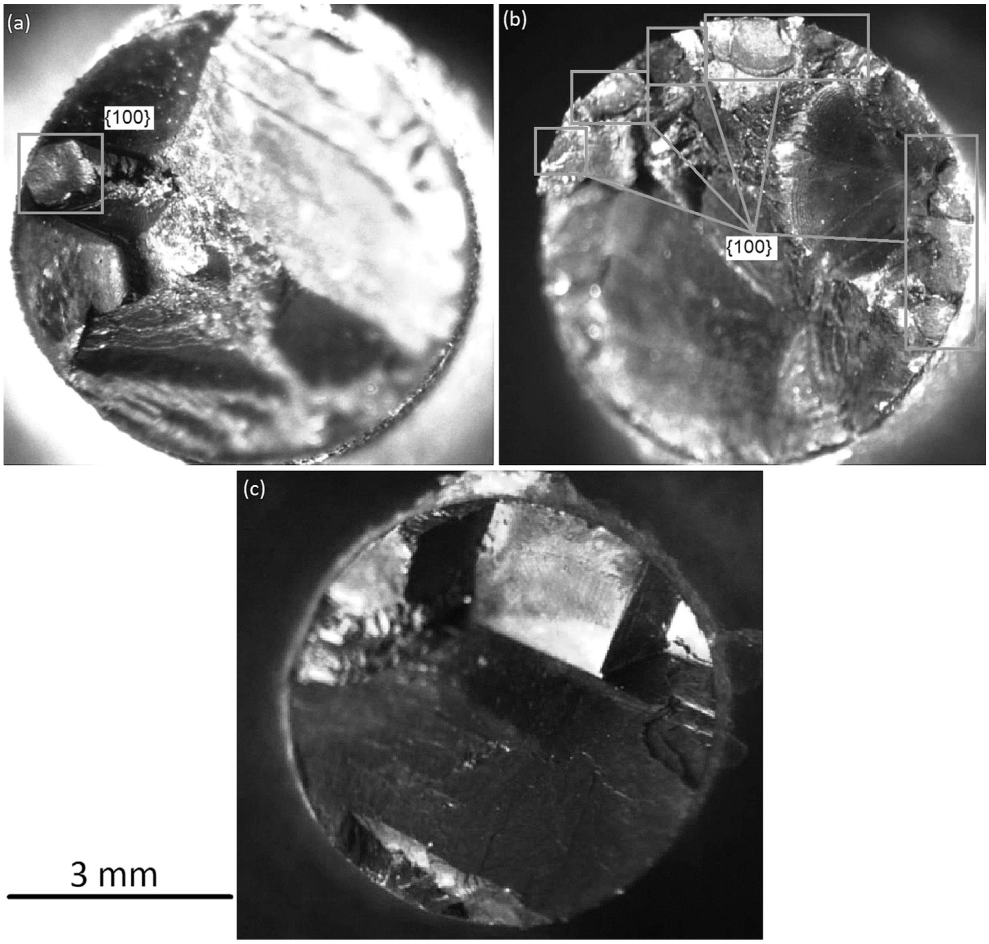

Fig. 9. Optical images of plain specimen fracture faces, (a) 800 MPa, 1-1-1-1 (s) trapezoidal loaded fatigue specimen, 500 h pre corrosion with 5 μg/cm^2/h flux at 550 °C, showing one {1 0 0} thumb nail fracture site, (b) 800 MPa, 1-60-1-1 (s) trapezoidal loaded fatigue specimen, 500 h pre corrosion with 5 μg/cm^2/h flux at 550 °C, showing multiple {1 0 0} thumb nail fracture sites, (c) 775 MPa, 1-1-1-1 (s) trapezoidal fatigue specimen, 500 h pre corrosion with 1.25 μg/cm^2/h at 550 °C, showing no optically visible {1 0 0} thumb nail fracture sites at this magnification.

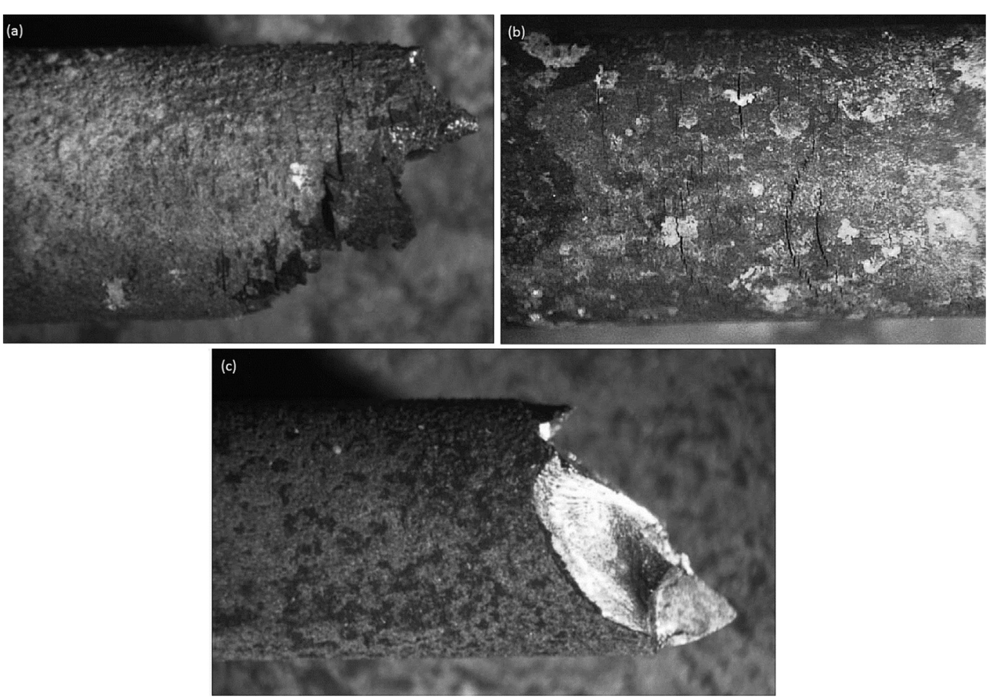

Fig. 10. Optical images showing side views of plain specimens after test exposures, (a) 800 MPa, 1-60-1-1 trapezoidal wave fatigue specimen, 500 h pre corrosion with 5 μg/cm^2/h flux at 550 °C, showing multiple cracks, (b) 900 MPa statically loaded 200 h specimen showing multiple cracks comparable with (a), (c) 725 MPa, 1-1-1-1 trapezoidal wave fatigue specimen, 500 h pre corrosion with 5 μg/cm^2/h flux at 550 °C showing one optically visible crack.

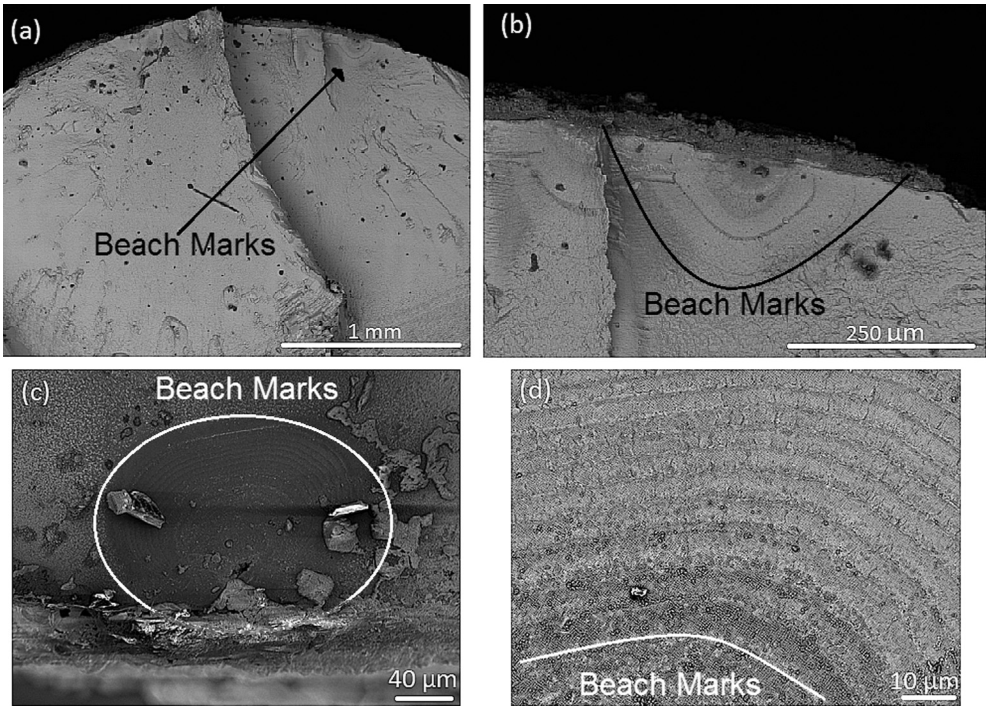

Fig. 11. SEM microscope images of fatigue specimen fracture surfaces, (a) 1-1-1-1 800 MPa, 500 h of 5 μg/cm^2/h pre corrosion showing beach type markings propagating from an initiation point, (b) 1-1-1-1 800 MPa, 500 h of 5 μg/cm^2/h pre corrosion at higher magnification showing ta smooth {1 0 0} crack plane with environmental markings, (c) 1-1-1-1 750 MPa, 500 h of 5 μg/cm^2/h pre corrosion showing smaller microscopic environmentally induced beach type markings propagating from an initiation point, (d) 1-1-1-1 750 MPa, 500 h of 5 μg/cm^2/h pre corrosion at higher magnification showing 5–10 μm jumps in environmentally induced markings.

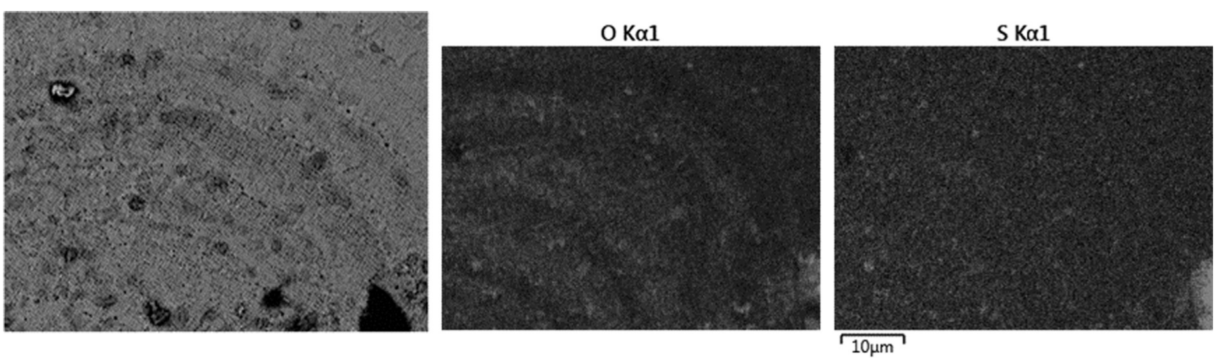

Fig. 12. SEM EDX mapping of a 1-1-1-1 800 MPa, 500 h of 5 μg/cm^2/h pre corrosion fracture face, showing some banding of oxygen and sulphur maps in correlation with microscopic environmentally induced beach mark type markings.

5. Conclusions

Type II hot corrosion combined with stress, results in a form of stress corrosion cracking, the mechanism was exacerbated by stress gradient. This mechanism initiates and propagates cracks on orthogonal {1 0 0} planes.

The presence of Type II hot corrosion also demonstrated an increase in the rate of fatigue propagation, similarly switching the crack propagation direction from ⟨1 1 1⟩ to ⟨1 0 0⟩ with higher salt deposition fluxes, demonstrating corrosion's influence in on the crack propagation plane.

Longer fatigue dwell periods of 1-60-1-1 and static stress cracking showed increased crack initiations when compared with more fatigue dominated mechanisms. This suggests that cracks could initiate and propagate under dwell periods during fatigue cycles.

Microscopy studies suggested a form of stress assisted type II embrittlement preferential to the γ' occurred at the crack tip.

A stress assisted SO_x gas induced fluxing mechanism at the crack tip was proposed to explain sulphate dependant crack tip embrittlement and ⟨1 0 0⟩ orthogonal propagation. More widely documented diffusion/absorption mechanisms for stress corrosion cracking (SCC), such as hydrogen embrittlement and stress assisted grain boundary oxidation (SAGBO) share similar characteristics. But they are not considered particularly active in SC CMSX-4 at these temperatures, and would not be dependent on sulphate fluxing like the mechanism presented in this paper demonstrated.

Micrograph studies of cracks suggest that the propagation mechanism in the more plastic γ channels may differ from that in the more brittle γ'. This resistance of the γ phase to propagation could suggests the importance of Cr in resisting the mechanism.

Further experimental and microscopy work is needed to properly understand the mechanism, specifically if and what species diffuses through the material and how, as well as what affect they have on the plasticity of the γ/γ′ microstructure.

Further work to record accurate crack propagation data is required to fully understand and quantify the effects of the mechanism in

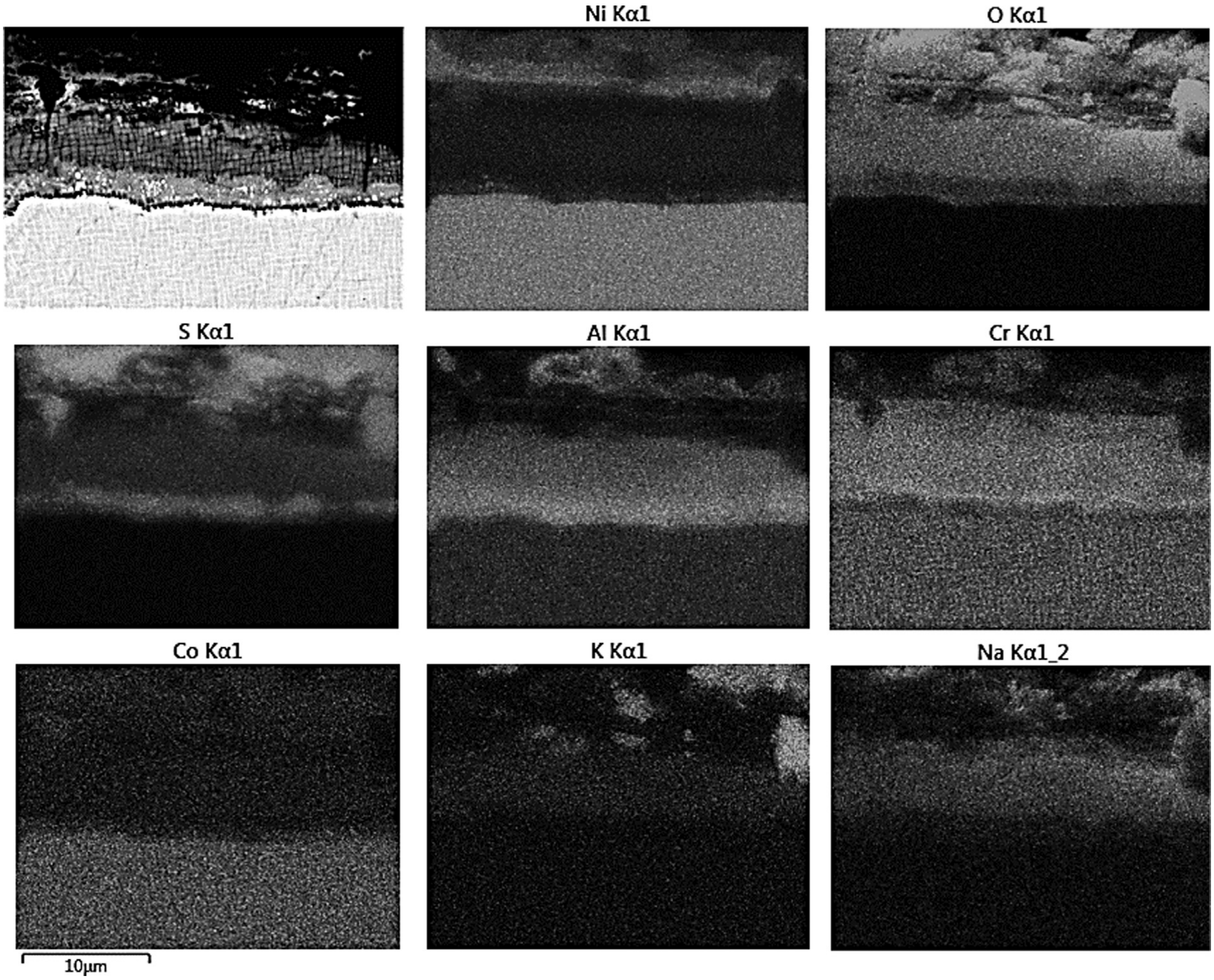

Fig. 13. SEM EDX mapping of a 1-1-1-1 800 MPa, 500 h of 5 μg/cm^2/h pre corrosion, corrosion fatigue product, this mapping is consistent with EDX mapping of statically loaded specimens and shows segregation in the corrosion products, forming an outer oxide scale of Ni/Co and an inner Cr/Al rich layer with a sulphur rich band reacting with the substrate interface.

Table 6
Fracture parameters calculated using FEA for 10 and 50 μm cracks in bodies loaded to a target stress of 800 MPa.

Geometry	Crack length (μm)	K_I (MPa·m$^{1/2}$)	LEFM geometry factor	Crack length needed to exceed K_{TH} (μm)
C-ring	50	10.8	1.08	96
	10	4.8	1.07	98
Plain specimen	50	10.07	0.99	114
	10	4.45	0.99	114
Three point bend	50	7.2	0.72	216
	10	3.33	0.74	204

relation to modelling, particularly at short crack lengths where cracks are more influenced by type II hot corrosion.

Acknowledgements

The authors acknowledge the support of the Engineering and Physical Research Council (EPSRC) for their support for the project - Flexible and Efficient Power Plant: Flex-E-Plant (Grant number: EP/K021095/1). They also thank the following partners for their the valuable contributions: GE Energy, Doosan Babcock Limited, Centrica plc., EDF Energy (West Burton Power) Limited., Uniper Technology Limited, Goodwin Steel Castings Limited, NPL Management Limited, R-MC Power Recovery Limited., RWE Generation UK plc., Scottish and Southern Energy (SSE) plc., Siemens Industrial Turbomachinery, and TWI Limited.

References

[1] ASM International. Hot corrosion in gas turbines. High Temp Corros Mater Appl 2007:249–58.
[2] Rosier H, Perkins K, Girling A, Leggett J, Gibson G. Factors affecting the corrosion fatigue life in nickel based superalloys for disc applications. MATEC Web Conf

2014;14:3001.
[3] Rahman MM, Ibrahim TK, Abdalla AN. Thermodynamic performance analysis of gas-turbine power-plant. Phys Sci 2011;6(14):3539–50.
[4] Harris K, Wahl JB. Improved single crystal superalloys, CMSX-4 (SLS) [La + Y] and CMSX-486. In: Superalloys 2004 (Tenth Int. Symp., no. Figure 1, p. 45–52, 2004).
[5] Birks N, Meier GH, Pettit FS. High-temperature corrosion resistance. JOM 1987;39(12):28–31.
[6] Eliaz N, Shemesh G, Latanision RM. Hot corrosion in gas turbine components. Eng Fail Anal 2002;9(1):31–43.
[7] Lortrakul P, Trice RW, Trumble KP, Dayananda MA. Investigation of the mechanisms of Type-II hot corrosion of superalloy CMSX-4. Corros Sci 2014;80:408–15.
[8] Brooking L, Sumner J, Gray S, Simms NJ. Stress corrosion of Ni-based superalloys. Mater High Temp 2017;35(December):120–9.
[9] Siebörger D, Knake H, Glatzel U. Temperature dependence of the elastic moduli of the nickel-base superalloy CMSX-4 and its isolated phases. Mater Sci Eng A 2001;298(1–2):26–33.
[10] Rengara B, Baba S, Okazaki M. Influence of crystal orientation on cyclic sliding friction and fretting fatigue behavior of single crystal ni-base superalloys. In: Superalloys 2016: Proceedings of the 13th international symposium on superalloys, 2016. p. 395–404.
[11] Sass V, Glatzel U, Feller-Kniepmeier M. Creep anisotropy in the monocrystalline nickel-base superalloy CMSX-4. In: Superalloys 1996 8th Int Symp Superalloys, 1996. p. 283–290.
[12] Joyce MR, Wu X, Reed PaS. The effect of environment and orientation on fatigue crack growth behaviour of CMSX-4 nickel base single crystal at 650 °C. Mater Lett 2004;58(1–2):99–103.
[13] Jianting G, Ranucci D, Picco E. Low cycle fatigue behaviour of cast nickel-base superalloy IN-738LC in air and in hot corrosive environments. Mater Sci Eng 1983;58(1):127–33.
[14] Mahobia GS, et al. Effect of hot corrosion on low cycle fatigue behavior of superalloy IN718. Int J Fatigue 2014;59:272–81.
[15] Nazmy MY. The effect of environment on the high temperature low cycle fatigue behaviour of cast nickel-base IN-738 alloy. Mater Sci Eng 1982;55(2):231–7.
[16] (Westinghouse Combustion Turbine Systems) Allen JM, (Westinghouse Reaserch and Development Center) Whitlow GA. Observations on the interaction of high mean stress and type II hot corrosion on the fatigue behavior of a nickel base superalloy. J Eng Gas Turbines Power, vol. 107, 1985. p. 220–4.
[17] De Marrocos P, Pais AR. Influence of stress state on high temperature fatigue crack growth, 2001. p. 127–135.
[18] Rezazadeh M, Alizadeh M, Fathi A. Turbine blade temperature calculation and life estimation - a sensitivity analysis. Propuls. Power Res. 2013;2(2):148–61.
[19] Anderson TL. Fracture mechanics: fundamentals and applications 2012;58:1.
[20] Donahue JR, Lass AB, Burns JT. "The interaction of corrosion fatigue and stress-corrosion cracking in a precipitation-hardened martensitic stainless steel. npj Mater Degrad 2017;1(1):11.
[21] Henaff G, Marchal K, Petit J. On fatigue crack propagation enhancement by a gaseous atmosphere: Experimental and theoretical aspects. Acta Metall Mater 1995;43(8):2931–42.
[22] Wu XJ, Miller M, Zhang Z, Miller J, Reed PAS. Fracture mechanics analysis of notch fatigue of a single crystal superalloy—CMSX-4. Icf11 2005;6:10.
[23] ISO 7539-5. Corrosion of metals and alloys - Stress corrosion testing - Part 5: Preparation and use of C-ring specimens; no. 1:1989.
[24] British Standards Institutions. BSI Standards Publication Plastics — Determination of flexural properties; 2013.
[25] Image-J. Oxford Instruments, 2017.
[26] AZtec. Oxford Intsruments, 2015.
[27] ANSYS Workbench 15.0. ANSYS, 2013.
[28] Abaqus/CAE. SIMULA, 2017.
[29] Dowling NE. Mechanical Behavior of Materials. 4th ed. Boston, MA: Pearson; 2012.

Effect of stress state and simultaneous hot corrosion on the crack propagation and fatigue life of single crystal superalloy CMSX-4

Brooking, Laurie

2018-05-03

L. Brooking, S. Gray, J. Sumner, et al., Effect of stress state and simultaneous hot corrosion on the crack propagation and fatigue life of single crystal superalloy CMSX-4. International Journal of Fatigue, Volume 116, November 2018, Pages 106-117

https://doi.org/10.1016/j.ijfatigue.2018.05.002